

Supporting Information: “Flux-induced topological superconductivity in full-shell nanowires,” by S. Vaitiekėnas *et al.*, Science (2020).

This document provides further information on:

1. Procedures used for nanofabrication of normal-insulator-superconductor (NIS) devices,
2. Details of procedures used for fabrication of Coulomb blockade (CB) devices,
3. Details of procedures used for measurement of normal-insulator-superconducting (NIS) devices,
4. Details of procedures used for measurement of Coulomb blockade (CB) devices,
5. Additional information on lever arm measurements for CB data,
6. Selection criteria for CB data and further analysis of CB data, including data that was previously unanalyzed or rejected before analysis,
7. Information about the behavior of other measured wire batches, including examples of representative devices.

Regarding items 1-4, we note that procedures for fabrication and measurement were developed over the course of the experiment, and so were not followed strictly from beginning to end and deviated particularly in the earlier runs. The procedure also evolved intentionally over the course of the experiment as we sought to explore ranges of behavior, new wire batches, and alternative device designs to flesh out the discovered phenomena. Given the evolutionary and exploratory character of this work, we do not recommend interpreting the variation in outcomes in terms of yield statistics. Measuring yield would require protocols where fixed procedures were repeated and statistics gathered, which was not carried out.

1. Procedure for NIS fabrication:

For the early measurements, fabrication began with wire selection. This was for wire batches 439, 637, and 638. The wire batch numbers reflect the growth count, numbered consecutively. Growth strategies and wire parameters differed from batch to batch. Wire batch 439 was grown from unpatterned Au catalyst droplets, leading to a relatively larger variance of diameters. In contrast, wire batch 829 used a patterned catalyst. Some batches were grown vertically quickly and then fattened with lateral growth to avoid dislocations. Al thickness varied batch-to-batch by design. None of the batches used were attempted exact repeats.

Wires were selected roughly from the middle of the growth substrate. Wires were transferred onto cleaved Si/SiO_x chips with prefabricated Ti/Au bond pads, meanders, and alignment marks using a micromanipulator with a 100 nm tungsten needle. An adhesion promotor, AR300-80 was spun, baked, and rinsed. This was found earlier to improve etch running, which was important to have the etch match the lithographic pattern. Parameters of the adhesion promoter step such as spin speed, bake time, and rinsing procedure, which may have important consequences, were not investigated.

For the etching step, a double layer of EL-6 MMA e-beam resist was spun and soft-baked (each layer) at 115 C for 1 min. Next, the etching windows were exposed by electron beam lithography, developed using MIBK and IPA, and cleaned with an oxygen plasma. Plasma cleaning is a critical step, removing residual polymer from the etch windows, but it was not optimized. The resist was then re-baked for another 1 min at 125 C. Next, the chip was etched in MF321 for 75 s, followed by a two-step quench in deionized water. The resist was then stripped, and a new resist layer was spun and soft-baked. This was a double-layer resist system consisting of A4 and A6 PMMA e-beam resist stack. The leads and contacts to the shell were exposed and developed (as before, rinsing and oxygen-plasma cleaning), then milled with RF Ar plasma (25 W, 9 min), then the Ti/Au (5/210 nm) leads were deposited, followed by a liftoff step. Another layer of A-6 was then spun and soft-baked. The leads were then written by electron beam lithography to expose the InAs core—same development step. Again, RF Ar milling, but at lower power (15 W, 6.5 min) to reduce damage to the InAs. Argon milling was calibrated weekly to ensure uniformity and correct milling time, which was crucial not overly to damage the InAs. Leads were metalized with Ti/Au (5/180 nm) and lift-off. After this, the wires were imaged using a scanning electron microscope for the first time.

Over the course of the experiment, this recipe evolved somewhat. For example, some devices have a top gate (Device 04), which required two additional fabrication steps. The first was a global layer of HfOx (8 nm) deposited by atomic layer deposition, followed by e-beam patterning of the top gate and deposition of Ti/Au (5/150 nm) top gates with new meanders deposited.

These procedures were developed over several years mostly on half-shell wires. We cannot say if each step was necessary or how changes affected device behavior or fabrication yield. The change from Transene D (Al etchant), used in early experiments, to MF321, was made because the 7 s etch with Transene D was more aggressive and too difficult to control and prevent over- or under-etching. One extra second made a significant difference. Also, Transene D was slower to etch the tough oxide surface, and then when it broke through in a statistical process the pure Al underneath was etched almost immediately. This means that the 7 s etch was dominated by the statistical process of breaking through the oxide. The more aggressive Transene D etch possibly caused more damage to the semiconductor. Overall, MF321 proved superior for most applications.

For other wire batches, this procedure was followed with slightly different MF321 etch times.

2. Procedure for CB fabrication:

The same fabrication procedure used for the NIS devices was followed for the CB devices, with a few differences: First, only 439 wires were used for the CB studies. Second, there was only one contacting step, which was the A6 resist step with the

lower-power Ar milling. Third, side gates were deposited in a separate A6 resist step, this time without milling (because no contact was made). Also, devices were imaged after etching and before the first deposition step. This was necessary because precise alignment was needed for the CB devices. It is known that imaging devices change the gate voltage pinch-off characteristics. Other possible effects of imaging are not known.

3. Procedure for NIS measurement:

Following wire bonding to an in-house designed circuit board, the sample was placed into a loading puck associated with a Bluefors XLD dilution refrigerator. RF and RC low-pass filters (QDevil) were installed in the fridge, and additional RC low-pass filters were installed in the puck. The overall source-drain line resistance from the sample to room temperature was roughly 13.4 k Ω .

Typically, each chip contained 10-15 devices, sometimes from different wire batches, and all devices could be bonded using a custom multilayer circuit board with 100 bond pads. Circuit boards similar to our design are available commercially (QDevil). All devices were grounded during bonding, mounting, loading, and cooling. The chip was cooled in the dark, without LED illumination. After reaching base temperature (roughly 12 hours after loading) and ungrounding the sample, continuity checks were performed using a lock-in amplifier in manual operation rather than under computer control. Most devices passed this continuity test. In the case where the continuity test failed, further measurement of that device was discontinued.

In the initial device screening phase, multiple devices were connected, each to a separate lock-in. Wires were not precisely oriented on the chip and so a parallel magnetic field could not be applied during the screening phase. Working at zero magnetic field, we looked for the complete pinch-off regime as a function of back-gate voltage. An example is shown in **Fig. 1**. Back-gate sweeps affect all wires on a chip. Pinch-off curves were taken for all working devices on a chip.

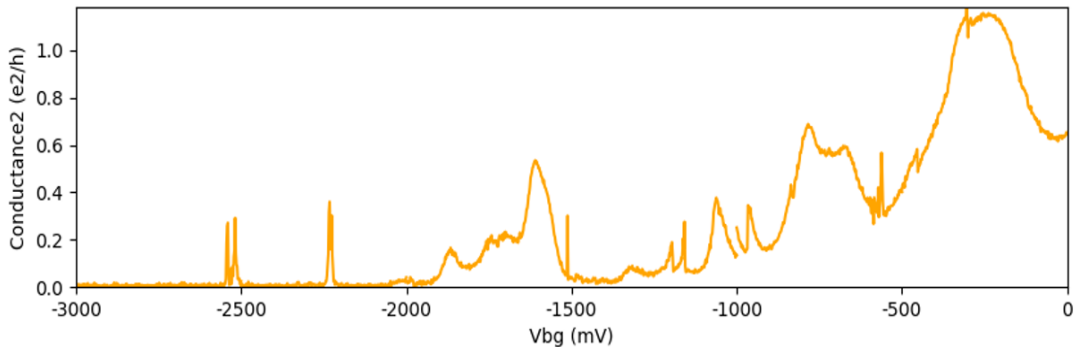


Fig. 1. Pinch-off curve. Conductance versus back gate voltage for Device 1.

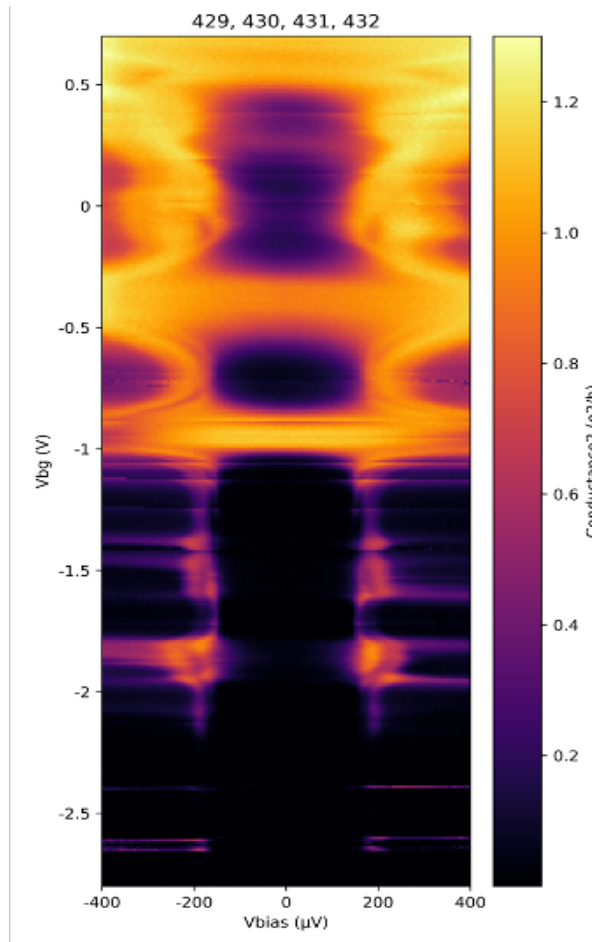


Fig. 2. Finding the tunneling regime. Conductance versus source-drain voltage and back-gate voltage at zero magnetic field.

Next, conductance, dI/dV , as a function of dc source-drain voltage and back gate, was measured, looking for the tunneling regime. An example is shown in **Fig. 2**. This was done for all working devices on the chip.

Next, a wire to focus on was selected based on the quality of the tunneling regime. A procedure for field alignment was carried out for that wire. That involved measuring the angle of the wire on the chip from the micrograph and using the data-acquisition computer controlling the magnet to define field directions in the coordinates of the wire. Fine-tuning of wire angle was typically not needed. For a given wire batch, the lobe structure was mapped out by measuring dI/dV as a function of parallel magnetic field and source-drain voltage. For subsequent wires on that batch, a full-lobe sweep at this stage was typically not repeated. Instead, it was enough to move to the center of the first lobe, knowing the rough field value for a given wire batch, and repeated the back-gate and source-drain measurement from pinch-off—defined as the condition $dI/dV \sim 0$ (unmeasurably small) independent of source-drain voltage—to the open regime, where $dI/dV > 2e^2/h$ at zero source-drain voltage. An example is shown in **Fig. 3**. This procedure was repeated for all wires on each chip.

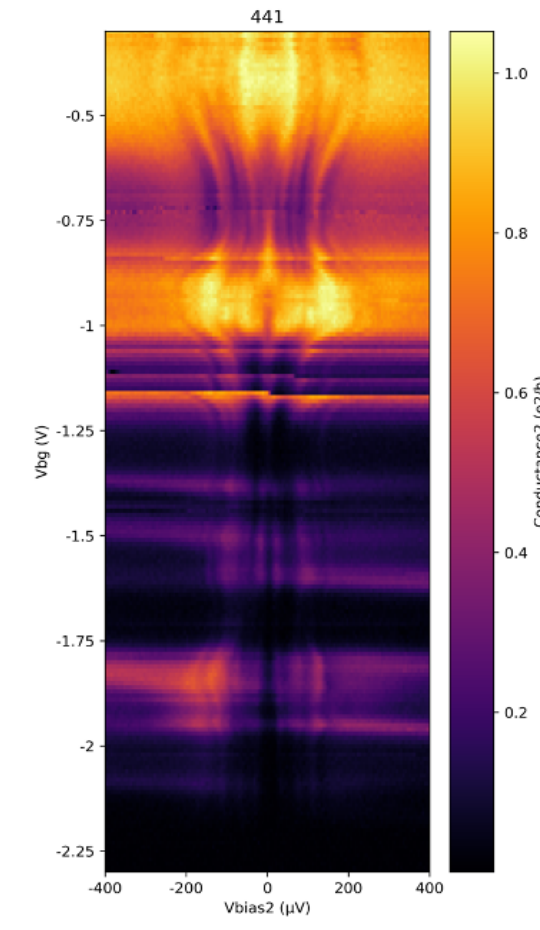


Fig. 3. Conductance versus source-drain voltage and back gate in the first lobe.

Next, zero-field data was examined to locate a good tunneling regime, that is, a regime with conductance smaller than the open regime, i.e., in the vicinity of $dI/dV \sim 0.05 - 0.2 e^2/h$, measured above the gap, with vanishing dI/dV below the gap, and at a less negative gate voltage than where many resonances (extending above and below the gap) were typically found.

The rationale behind this part of the procedure was that reduced screening at strong depletion typically results in multiple potential maxima along the junction. In looking for a tunneling regime, the goal was to avoid multiple barriers along the junction. Only in that case, and for weak tunneling ($< \sim 0.3 e^2/h$), is tunneling current proportional to the local density of states, as discussed by Blonder, Tinkham, and Klapwijk (BTK). The local density of states is the quantity of interest in these studies.

Multiple barriers from weak screening *generically* create quantum dots (QDs) whose signatures are resonances. In fact, at low density, resonances may form even in the absence of disorder. This does not require fine-tuning, only an awareness that QDs mean that conductance is not proportional to the local density of states. The tunneling regime in modestly disordered junctions is, therefore an intermediate

condition: if the junction is too open, dI/dV is not proportional to the local density of states *a la* BTK; if the junction is too closed, reduced screening typically leads to resonances and disordered transport. Tuning tunnel barriers for the tunneling regime and avoiding quantum dots is a familiar part of mesoscopic physics, used whenever gate-controlled tunable barriers are needed for spectroscopy. In highly disordered junctions (or in case of poor contacts), many barriers in series give rise to a different effect, dynamical Coulomb blockade, a reduction of conductance around zero bias lacking periodic gate response. While essentially all devices showed a QD regime near pinch-off (i.e., gate voltages more negative than the tunneling regime), for some wire batches or individual devices, dynamical Coulomb blockade was observed on top of any lobe structure. This feature, along with other signatures of strong disorder such as gate hysteresis, was taken to be a sign that something had gone badly with the junction during fabrication, and typically further measurement on that device was discontinued.

Next, on devices with an accessible tunneling regime—meaning that the device had a relatively resonance-free region below the open regime without strong, frequent resonance or dynamical Coulomb blockade—higher-resolution data were taken in the zeroth and first lobes, over the range from the open regime to the QD regime, spanning the tunneling regime (**Fig. 4**).

Next, high-resolution magnetic field sweeps were taken at a few representative back-gate values within this range of back-gate voltages found above. Typically, 1-3 values of back-gate voltage were examined (**Fig. 5**).

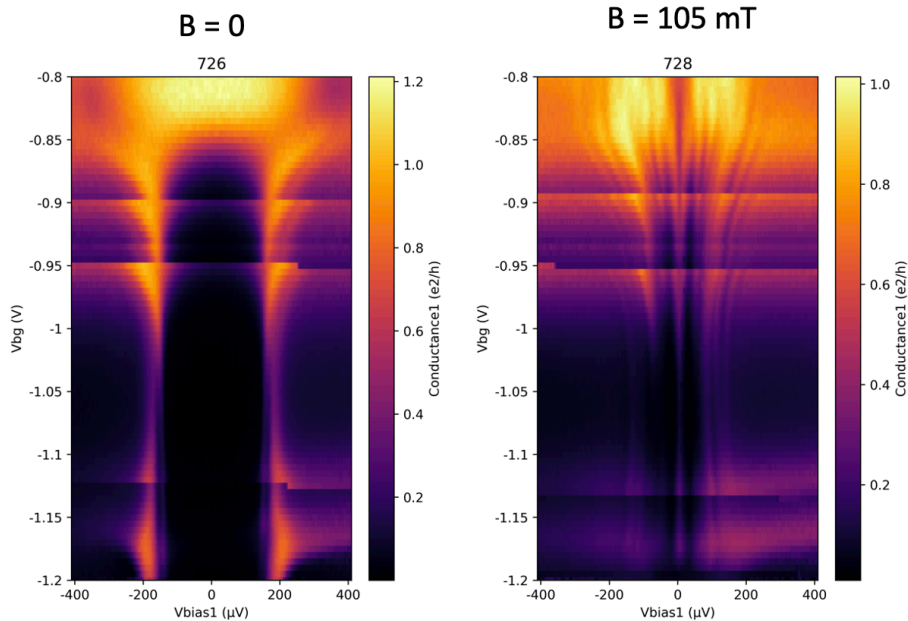


Fig. 4. High resolution scans of conductance versus source-drain voltage and back gate at zero field and in the middle of the first lobe.

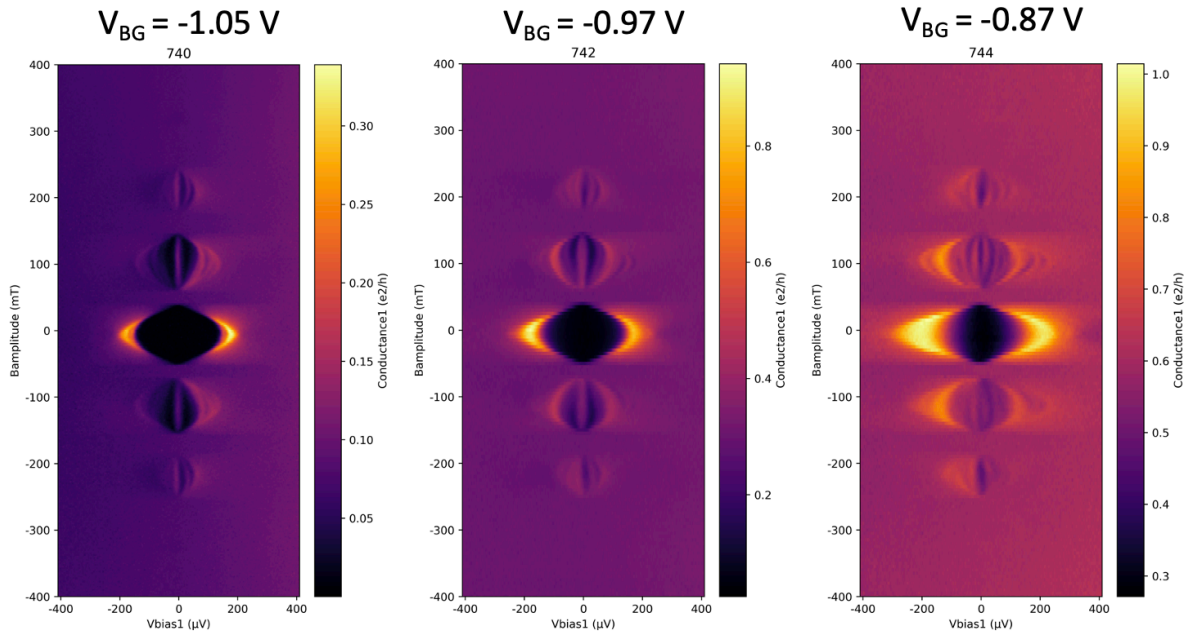


Fig. 5 Conductance as a function of source-drain voltage and axial magnetic field at three back gate voltages.

For devices that did not show a good tunneling regime (e.g., most devices from wire batches 637 and 638, for unknown reasons), measurements were either discontinued or a few field sweeps were taken at gate-voltage values between resonances.

4. Procedure for CB measurement:

The availability of full-shell wires of length 10 μm allowed multiple devices to be fabricated on the same wire. This was important given the known quantitative variability among devices that were qualitatively the same, including devices from the same wire batch (for instance, Device 1 and Device 3). Multi-island devices were designed with two contacts and three side gates per island in addition to a global back gate, allowing the two tunnel barriers and island occupancy to be independently controlled. The four gates acting on each island are denoted *left*, *right*, *plunger*, and *back*. The procedure that was followed aimed to compare multiple islands measured on the same wire. We began by looking for devices with all island segments working.

Each chip contained up to four bonded devices. Within a cooldown, devices were measured island-by-island using manual lock-in measurements to check for continuity and gateability. The first chip with CB devices that was cooled had no CB devices with all segments working. Non-working means failing the continuity test and cannot be turned on with the side or back gates. These devices were not measured further. On the second chip with CB devices, one of the three devices checked on that chip during the first cooldown had all islands working. The other two had non-

working islands. On a subsequent cooldown, a fourth device was examined. It also had a non-working island and was not measured further.

Each island on the all-working device on the second chip immediately showed gross features of CB, i.e., oscillations of conductance as a function of any of the gate voltages.

One at a time, each island was tuned into a symmetric weak-tunneling regime by tuning four gates per island. The procedure is illustrated with data for the shortest island (200 nm length) the same process was carried out serially for all segments. First, the back gate was swept until valley conductance vanished, as shown in **Fig. 6**. Next, the source-drain offset was zeroed (numerically) by examining conductance versus source-drain and plunger-gate voltages (**Fig. 7**). Next, the back gate was used to pinch off the island by sweeping until the CB peaks vanished (**Fig. 8**). At that value of back gate, the device was next symmetrized by examining sweeps of left and right gates (**Figs. 9, 10**), noting that this generally resulted in unequal voltages on left and right gates. Tuning left and right gates over large ranges revealed slowly varying nonmonotonic conductance, presumably due to resonances in the leads. The device was tuned for a rough maximum of peak height to find the rough diagonal where left and right gates had equal influence avoiding these nonmonotonic regions in left-right

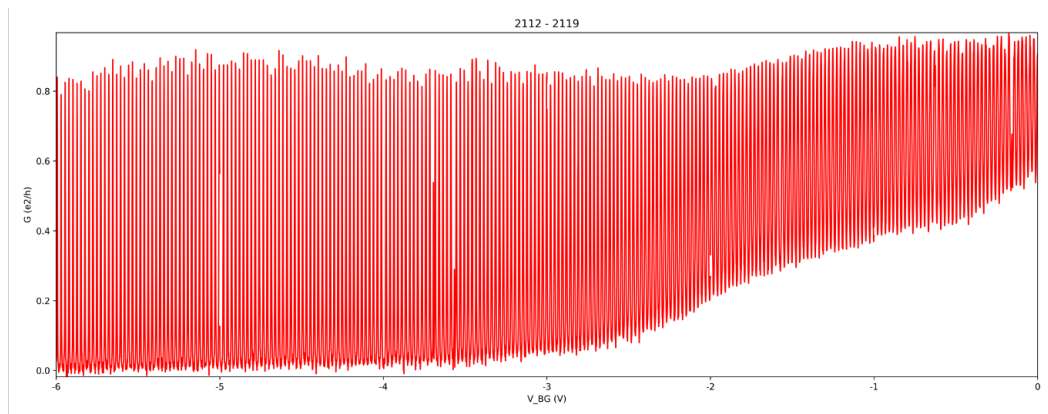


Fig. 6. Initial sweep of back gate to tune an island.

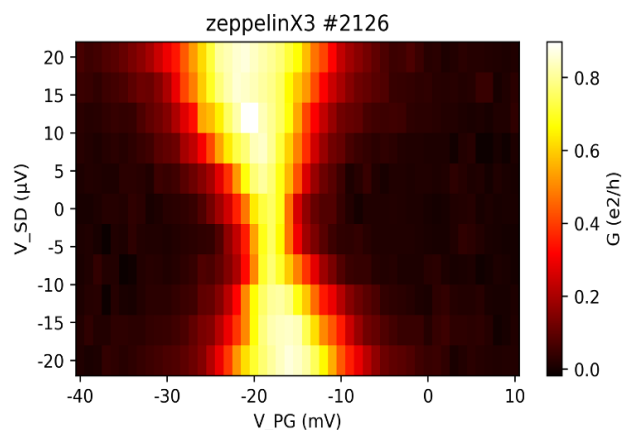


Fig. 7. Correcting source-drain bias offset.

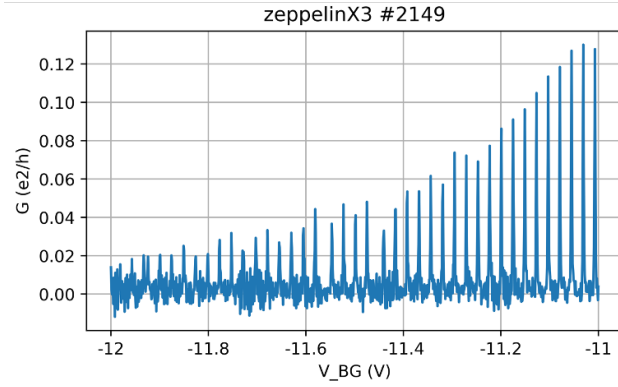


Fig. 8. Back gate pinch off. Conductance versus back gate.

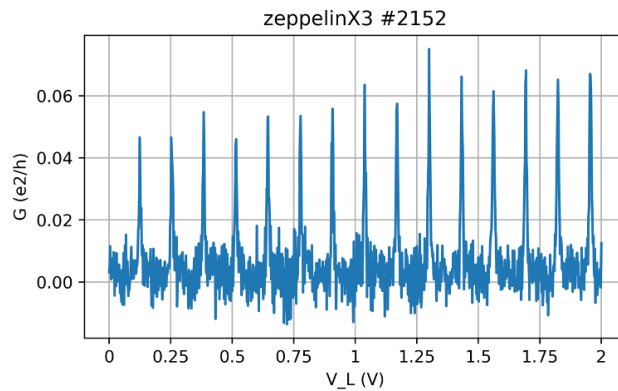


Fig. 9. Turning conductance back on with left gate.

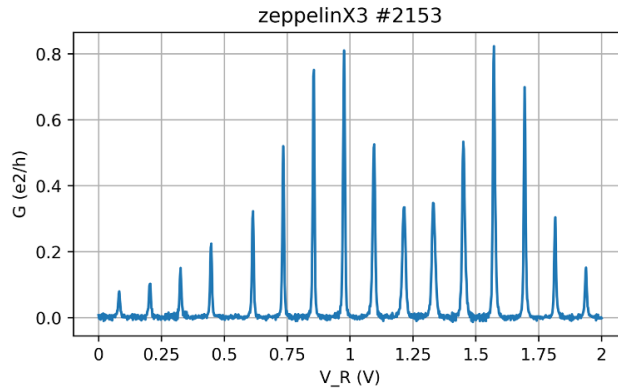


Fig. 10. Turning conductance back on with right gate.

gate space. A typical large-range sweep of left gates is shown in **Fig. 11**. This procedure is typical of how quantum dots are tuned in a variety of contexts.

After symmetrizing left and right conductances and avoiding nonmonotonic regions, a window of peaks was examined to find regimes in the plunger gate where the peak valleys went to zero conductance, peaks were moderately high (roughly $0.4\text{-}0.8 e^2/h$), see **Fig. 12**. This completes the island tune-up for one island.

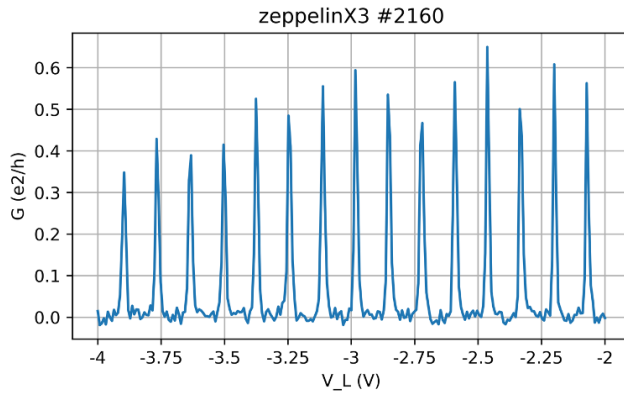


Fig. 11. Long-range left gate sweep.

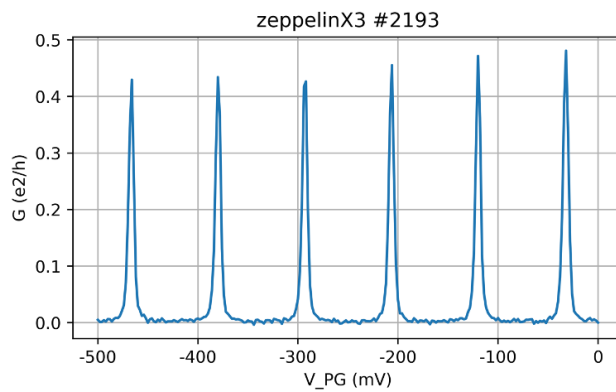


Fig. 12. Plunger gate sweep. Conductance versus plunger gate.

Tuning-up was carried out at zero magnetic field. Next, plunger gate sweeps on the tuned island were carried out at zero field, in the destructive regime, and in the middle of the first lobe (**Fig. 13**). The magnetic field was aligned to the wire axis following the same procedure as in the NIS devices, based on micrographs of the device. (Minor curvature of wires was not accounted for). The field magnitudes for the destructive regime and first lobe were known from previous measurements on the same wire batch. This was carried out as a check, which all segments passed.

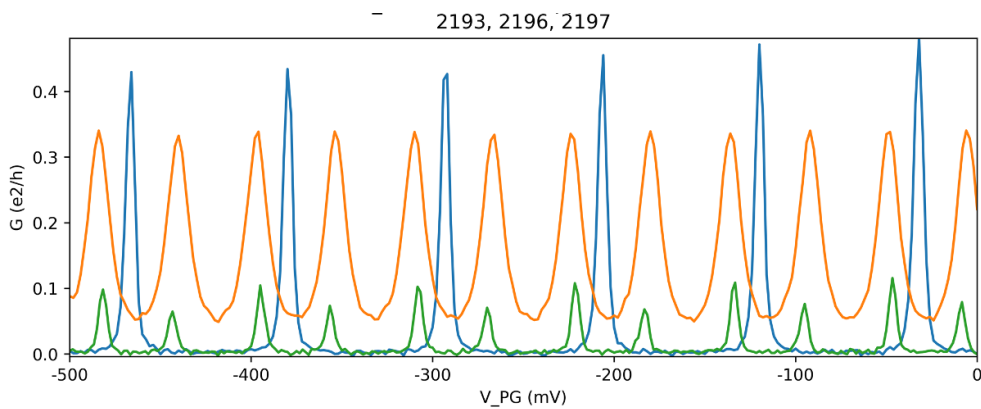


Fig. 13. Plunger gate sweep on the 200 nm island at zero field showing $2e$ peak spacing (blue), destructive regime showing precise $1e$ peak spacing (orange), and in the middle of the first lobe, showing even-odd peak spacing (green).

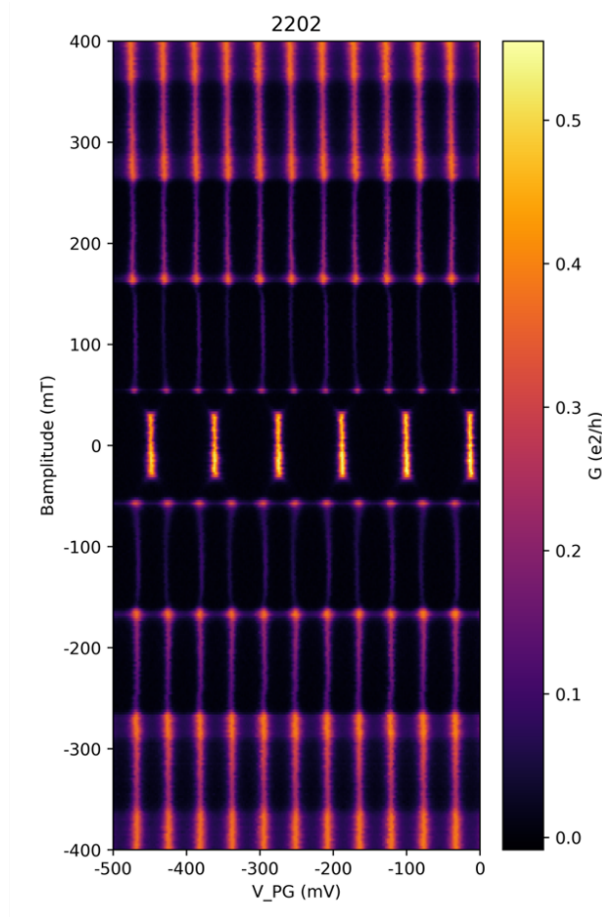


Fig. 14. Conductance as a function of plunger gate and axial magnetic field for 200 nm island.

Next, a high-resolution map of dI/dV as a function of magnetic field (outer loop) and plunger gate voltage (inner loop) was taken, spanning roughly 6-10 CB peaks, as illustrated in **Fig. 14**. These runs typically took several hours and swept continuously from positive to negative field. The symmetry of the data in magnetic field provided a further check on device stability.

Immediately after the field sweep, without changing gate voltages, conductance was measured as a function of source-drain voltage (inner loop) and plunger gate (outer loop). These “CB-diamond” runs (**Fig. 15**) provided a measure of the lever arm of allowing gate sweeps to be converted to energy. The fact that island energy levels detected by CB measurements depend sensitively on the lever arm, *though the mean CB spacing does not*, motivated taking separate measurements of CB diamonds in the zeroth lobe, the destructive regime, and the first lobe. The CB diamonds in the first lobe were especially important for converting peak spacing to energy. This conversion allowed different islands to be compared. Diamonds were taken at the value of the magnetic field where the peak spacing cuts were extracted from the 2D maps. Separate lever arms for the source and drain were extracted from leading and trailing diamond edges to compensate for any remaining asymmetry in the coupling of the island to the two leads. **Figure 15** also shows the discrete subgap spectrum in

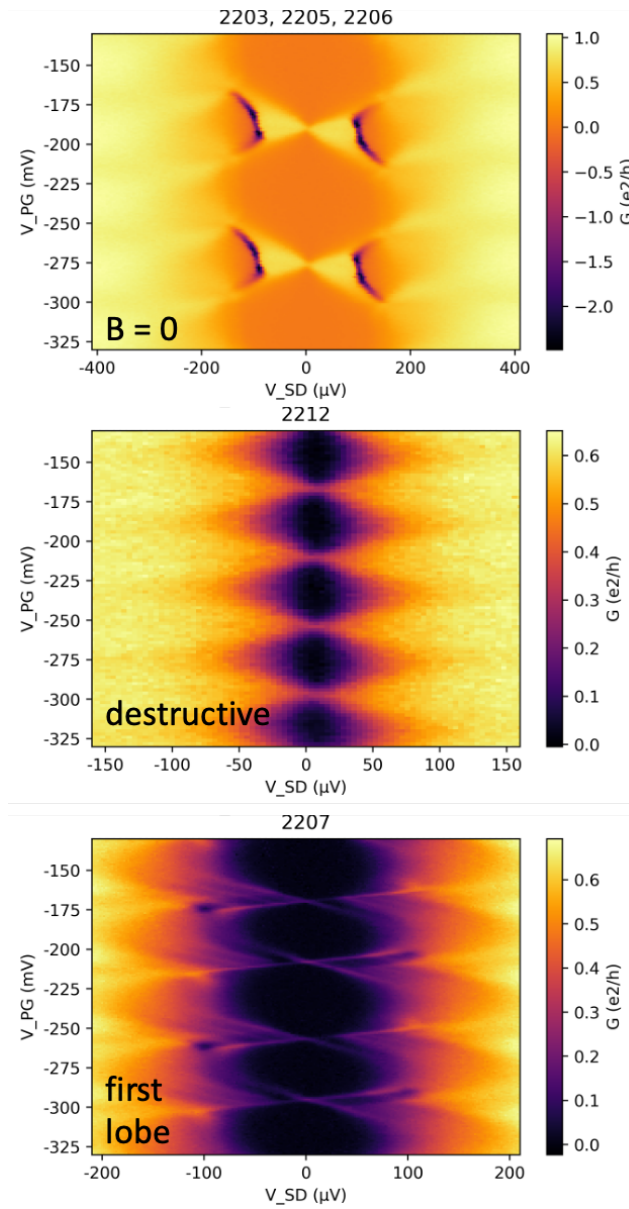


Fig. 15. Conductance as a function of source drain voltage and plunger gate at zero field (top), destructive regime (middle), and middle of the first lobe (bottom), used to measure lever arm. Note discrete subgap spectrum in the first lobe.

the first lobe. This important feature is not visible in linear response (zero dc source-drain voltage) CB blockade data. **Figure 15** also shows that CB diamonds in the destructive regime were blurred, as expected for metallic islands, making it difficult to extract a lever arm there.

To increase statistics for each island, the procedure was repeated at 1-2 additional back gate voltages (with corresponding required tune-up of left and right gates).

For the 200 nm, 300 nm, 400 nm, and 600 nm islands, peak spacing fluctuations were extracted from the 2D maps of field and gate voltage. Then, CB diamonds measured in the first lobe were used to convert peak spacing to energy.

For the 800 nm and 1000 nm islands, where peak spacing was nearly uniform in the first lobe, plunger sweeps at very high resolution were taken at several discrete values of the magnetic field in the first lobe. For the 1000 nm island, increased statistics were obtained by repeating the 110 mT high-resolution sweep at one other back gate voltage (with re-tuned left and right gates). Data at 110 mT and 140 mT were further analyzed using the first-lobe lever-arm data from 110 mT to test the dependence of island-length scaling on the field-dependent gap.

5. Lever Arm Measurement

As described in the main text, lever arms, η , which were used to convert peak spacings as a function of plunger gate to energy units, were extracted for each Coulomb island separately. Moreover, as described below, using multiple runs to generate spacing statistics required extracting lever arms for each gate configuration where spacings were measured.

It is important to note that the lever arm is *not* a purely geometrical quantity. It depends on the self-capacitance of the island, which in turn depends on lead transmission. The physics of the lead-coupling effect (elastic cotunneling and quenched charging energy) on the lever arm was studied theoretically by Aleiner *et al.* [Phys. Rev. B **57**, 9608 (1998)] and Kaminski *et al.* [Phys. Rev. Lett. **81**, 685 (1998)], and experimentally by Maurer *et al.* [Phys. Rev. Lett. **83**, 1403 (1999)] and a number of papers since. Because average peak spacing as a function of gate voltage is not sensitive to η —the result of a cancellation of total capacitance in the peak-spacing voltage scale—it is tempting not to consider the lever arm carefully. However, as discussed in Maurer *et al.* [Phys. Rev. Lett. **83**, 1403 (1999)] and elsewhere, extracting the position of energy levels *within* the island depends sensitively on η . Therefore, careful measurement of the level arm from Coulomb diamonds is as important as careful measurement of peak positions.

Our procedure was as follows:

- Lever arms were measured *after* the island was tuned up.
- For *each* of multiple runs for each island length, lever arms were extracted from the 2D maps of conductance as a function of gate voltage and source-drain bias *at the value of magnetic field where the corresponding peak-spacing data were taken*, that is, at 110 mT. This was described in the Supplementary Material (page 9ff). We note that it would *not* have been appropriate to extract lever arms at zero field and then use that value for the first-lobe peak spacing because lever arms may depend on field.

- For each run, the lever arm was found by drawing a straight line along the Coulomb island conductance-resonance ridges, through zero, and measuring the slope of that line, as described in the caption of the Supplementary Material Fig. S17.
- Slopes of conductance ridges were measured separately for source (positive slope) and drain (negative slope). The two values were averaged following the method described in Ref. [67] of the paper.
- Lever arms found this way were measured for multiple Coulomb diamonds (from plunger gate voltage sweeps), and the results were averaged to yield an average lever arm *per run*. To emphasize: the average lever arm per run was over source/drain slopes and multiple Coulomb diamonds.
- As discussed in Supplementary Material page 9ff, multiple tunings of each length were used to increase statistics per island.
- For each island length, an overall average lever arm—that is, averaged over source and drain, multiple diamonds, *and* multiple tunings—is given in Table S1 in the Supplementary Material.
- Below, we provide additional information that might be of interest, namely, the lever arms extracted for each of the tunings.

Length (nm)	Run ID	Lever arm (meV/V)
200	3166	4.6
200	2207	4.2
200	2252	5.8
300	1889	6.1
300	1917	5.2
300	1936	7.4
400	3425	12.1
400	2047	10.5
600	192	19.3
600	202	15.7
800	470	16.7
1000	1472	14.5
1000	1534	15.8

6. Selection criteria for CB data

In addition to the CB peak-spacing data that were analyzed for the paper, there were a number of additional runs that were not previously analyzed (for instance, backup runs) or were excluded before analysis by various criteria, as noted in the table below. We emphasize that exclusion occurred *before* any peak-spacing analysis. We have now carried out peak spacing analysis on the previously excluded data (**Fig. 16**).

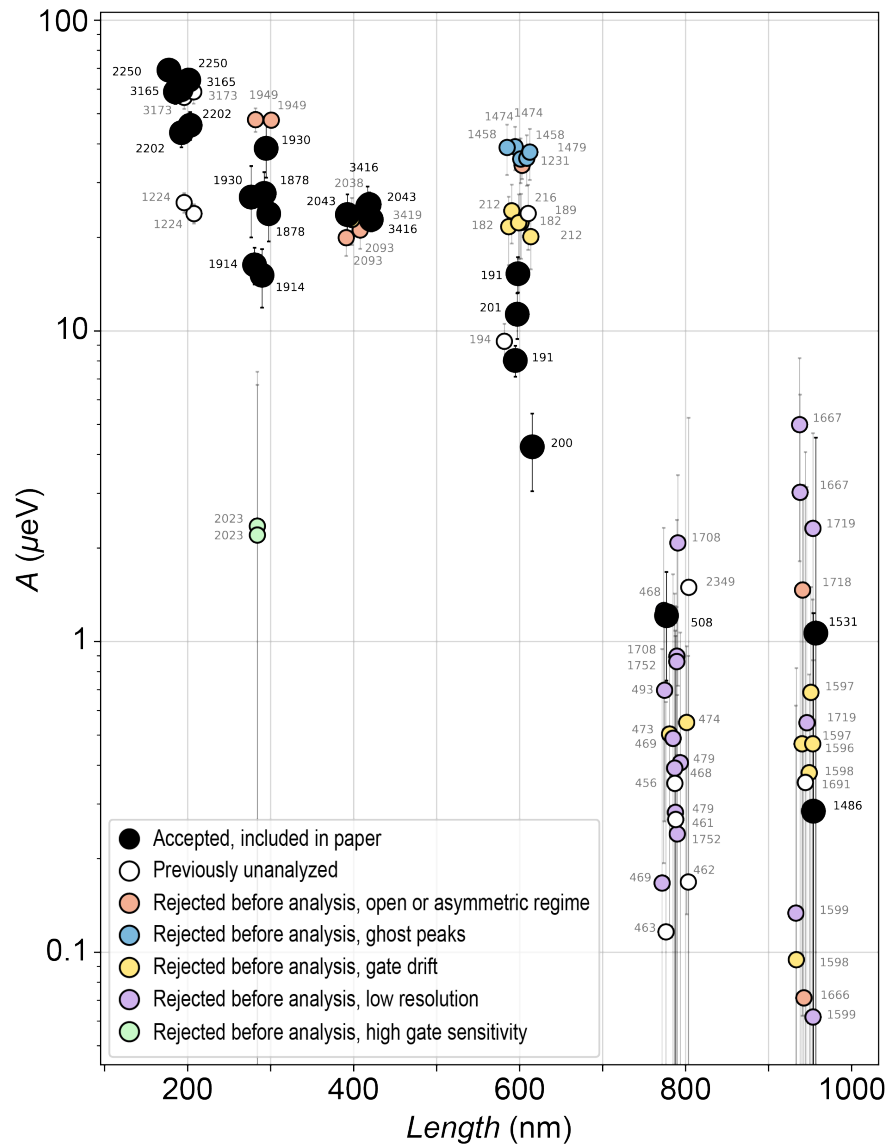


Fig. 16. Even-odd peak spacing difference converted to energy for datasets that had associated Coulomb diamonds for lever-arm measurements.

Length	First cool down, accepted	First cool down, not analyzed or rejected	Comments	Second cool down, accepted	Second cool down, not analyzed or rejected	Comments
200 nm	3165	3173	3173 appears to be a re-take of 3165. Associated diamonds in 3166.		1224	We cannot recall why these data were not analyzed. We suspect this was a backup run that we never got around to analyzing. Associated diamonds in 1223.

200 nm	2202					
200 nm	2250					
300 nm	1878	1949	Run 1949 has large conductance, outside of our usual range. In fact, the reason for the peak-height criterion is visible by eye in 1949: the exaggerated peak motion in the first lobe results from transmission contribution to total capacitance. In this case, peak motion does not represent density of states. Note that valley conductance was not fully suppressed (run 1948), and Coulomb blockade in the destructive regime was nearly absent (run 1946). Data is reasonably quiet, but not in a regime to measure DOS. Associated diamonds in 1952.	1930	2023	Run 2024, which is the associated gate sweep to 2023, showed strongly non-monotonic features. Associated diamonds in 2020.
300 nm	1914					
300 nm		1863	Lower-resolution calibration sweeps. No diamonds.			
300 nm		1907	Calibration sweep with finite conductance background in the Coulomb valleys. No diamonds.			
400 nm	3416	3419	Concerned with possible drift in 3416, run 3419 was a re-take of 3416, taken after measuring the diamonds with no gate-voltage changes. Associated diamonds in 3425.		668	The subsequent run 669 showed strange line shapes, which raised our suspicion. In any case, we already had enough data for this island. No diamonds.

400 nm	2043	2038	A large switch occurred in the middle of run 2038, which also had a drift, so 2043 was taken and analyzed instead. Associated diamonds in 2047.		763	We cannot recall why these data were not analyzed. We suspect this was a backup run that we never got around to analyzing. Associated diamonds in run 764.
400 nm					808	This was a backup run but showed jumps in the data. Associated diamonds in run 809.
400 nm					898	Only one side of magnetic field taken. Unusual switching behaviour at $V_{PG} \sim -140$ mV. No diamonds.
400 nm		2093	One switch visible. Zero-field Coulomb peaks have low conductance. Destructive regime displays high conductance indicating open regime or asymmetric tuning. Associated diamonds in run 2095.			
400 nm					654	1D sweep at 110 mT only. This lacks destructive regime data, which acts as calibration. No diamonds.
400 nm					929	1D sweep at 110 mT only. The sweep displays an irregular peak spacing at around -260 mV. We do not know if this is a jump in parity or in gating. No diamonds.
600 nm		1231	Because of the unusually high conductance in the destructive regime of run 1231, this did not follow the usual behavior and so was not pursued. Associated diamonds in 1235.	200	182	Large drift and shifting. Some switches. Associated diamonds in run 183.

600 nm		1458	Ghost peaks [Albrecht PRL] in the zeroth lobe indicate parity switching amplified by asymmetric barriers. Associated diamonds in run 1461.	201	189	189 was repeat of 182 (only one side of magnetic field) taken after the device became more quiet. Associated diamonds in run 183.
600 nm				191		
600 nm					194	194 was repeat of 191 (only one side of magnetic field) taken after the device became more quiet. Associated diamonds in 192.
600 nm					216	Note the large drift in 212, which was taken at the same gate settings. The associated diamonds in run 214 display a large asymmetry.
600 nm		1428	Sweep with finite conductance background in the valleys, taken during calibration. The associated zero field data shows low conductance as seen in 1425. No diamonds.			
600 nm		1430	Sweep taken during calibration. The associated zero-field sweep shows ghost [Albrecht PRL] peaks as seen in run 1432. No diamonds.			
600 nm		1474	Ghost peaks [Albrecht PRL] indicate parity switches. Several jumps including one in the middle of the first lobe. Associated diamonds in run 1476.			
600 nm		1479	Similar run to 1474 displaying ghost peaks [Albrecht PRL], suggesting parity switches. Associated diamonds in run 1476.			

600 nm		1111	Sweep displays low zero-field Coulomb peak conductance and a very high conductance in the destructive regime, indicating either an open regime or asymmetrically tuned barriers. In addition, based on the subsequent run 1112, it appears to be taken close to an end resonance. No diamonds.			
600 nm		1125	There is a large switch at roughly 130 mT. Also, the sweep displays low zeroth lobe peak conductance and high destructive regime conductance. No diamonds.			
800 nm				508	391	Large jump near the destructive regime. Only one side of the magnetic field. Low conductance in the zeroth lobe. No diamonds.
800 nm		1708	Low-resolution sweep inadequate for this length. In addition, the data display a drift and low peak conductance in the zeroth lobe. Associated diamonds in run 1712.		469	Drifting more than typical runs. Large jumps, including in the middle of both first lobes. Similar position indicates field driven jump. Associated diamonds in 465.
800 nm		1752	Low-resolution sweep inadequate for this length. In addition, the conductance is high in the destructive regime indicating an open regime. Associated diamonds in run 1754.		479	Low-resolution sweep inadequate for this length. Associated diamonds in run 477.
800 nm		2349	Coulomb peaks invisible in the zeroth lobe. The prior gate tuning did not follow the tune-up procedure. Associated diamonds in 2353.			

800 nm		1760	Several switch and drift. Run discontinued. No diamonds.			
800 nm					456, 461, 462, 463	These runs were used to develop the method of high-resolution one-dimensional sweeps. Associated diamonds in run 465.
800 nm					468, 469	Low-resolution sweep inadequate for this length. Also show significant switches. Associated diamonds in run 465.
800 nm					473, 474	Two back-to-back sweeps with different heights indicating drift not yet settled. Associated diamonds in run 470.
800 nm					493	493 was a low-resolution sweep, which was not analyzed further; higher resolution sweep 508, taken at the same settings, was used instead. Associated diamonds in run 470.
800 nm					539	Clear switch in the middle of the run. No diamonds.
1000 nm				1486		
1000 nm				1531		
1000 nm					1596-1599	After taking the high-resolution sweep 1596, the device was still drifting as seen in runs 1597-1599. Associated diamonds in run 1595.
1000 nm					1666, 1667	Not analyzed because of the very unusual behavior exemplified by the zero-field data in 1664. Associated diamonds in run 1665.

1000 nm					1691	At least two switches are visible by between the first and the second, and the fifth and the sixths Coulomb peaks. We do not know if these are jumps in parity or in gating. The procedure was not followed for the tune up and there is no information on the zeroth lobe. Associated diamonds in run 1690.
1000 nm					1718, 1719	This data is unusual, but similar to data in 1664-1667. Associated diamonds in run 1717 (including a switch).

7. Information about individual wire batches

QDev 439	Unsuccessful fabrication	Procedure not followed/ Not studied systematically	No clear spectroscopy	Clear spectroscopy, procedure not satisfied, no ZBP*	Clear spectroscopy, procedure satisfied, no ZBP	Questionable ZBP observed	Clear spectroscopy ZBP observed	Total number of devices
NIS-junctions	24, 34, 38, 40-42, 81-82	13-15	36, 39, 4J2		12		1, 3, 4J1, 8, 9, 10, 11	
Quantity	8	3	3	0	1	0	7	22

4J1 and 4J2 refer to device 4 junctions 1 and 2.

Devices 2, 6, 7, 35, 37, and 43 were CB-island devices.

Devices 44 through 53 were SIS and had large resistances.

*See "Table PNS".

QDev 637	Unsuccessful fabrication	Procedure not followed/ Not studied systematically	No clear spectroscopy	Clear spectroscopy , procedure not satisfied, no ZBP*	Clear spectroscopy, procedure satisfied, no ZBP	Questionable ZBP observed	Clear spectroscopy ZBP observed	Total number of devices
NIS-junctions	29	16-18, 26		19, 25, 27, 28				
Quantity	1	4	0	4	0	0	0	9

A different wire batch (QDev637) than the main batch (QDev439) studied in the paper. This batch had smaller diameter and thinner shell visible on micrographs. Non-destructive or no Little-Parks oscillations in the 4-probe measurements. Various end-dot and ZBPs were observed inconsistently. No ZBPs in the tunneling regime.

*See "Table PNS".

QDev 638	Unsuccessful fabrication	Procedure not followed/ Not studied systematically	No clear spectroscopy	Clear spectroscopy , procedure not satisfied, no ZBP*	Clear spectroscopy, procedure satisfied, no ZBP	Questionable ZBP observed	Clear spectroscopy ZBP observed	Total number of devices
NIS-junctions		30, 33	22	21, 31, 32	5, 20, 23			
Quantity	0	2	1	3	3	0	0	9

A different wire batch (QDev638) than the main batch (QDev439) studied in the paper. This is the same wire batch as Device 5 from the paper that did not show ZBPs in the tunneling regime. This batch had a smaller diameter and thinner shell visible on micrographs.

Device 22 could not be pinched off.

Device 30: Spectroscopy was not measured because 4-probe data showed a non-destructive Little Parks effect.

Device 33: Very little data because of poor spectroscopy.

*See "Table PNS".

QDev 564	Unsuccessful fabrication	Procedure not followed/ Not studied systematically	No clear spectroscopy	Clear spectroscopy, procedure not satisfied, no ZBP*	Clear spectroscopy, procedure satisfied, no ZBP	Questionable ZBP observed	Clear spectroscopy ZBP observed	Total number of devices
NIS-junctions	78, 79		75	71, 72, 74, 76, 77	73			
Quantity	2	0	1	5	1	0	0	9

A different wire batch (QDev564) than the main batch (QDev439) studied in the paper. Wires from this batch were used in Vaitiekenas, Krogstrup, Marcus, PRB 101, 060507(R) (2020). This batch had larger diameter and thicker shell visible on micrographs. Non-destructive Little-Parks oscillations in the 4-probe measurements. Subgap states were uncommon in these wires.

Device 75 could not be pinched off.

*See "Table PNS".

QDev 829	Unsuccessful fabrication	Procedure not followed/ Not studied systematically	No clear spectroscopy	Clear spectroscopy, procedure not satisfied, no ZBP*	Clear spectroscopy, procedure satisfied, no ZBP	Questionable ZBP observed	Clear spectroscopy ZBP observed	Total number of devices
NIS-junctions	60, 64, 66, 70	54-57	58	61	59, 63J2, 65, 68	0	63J1	
Quantity	4	4	1	1	4	0	1	15

63J1 and 63J2 refer to junctions 1 and 2 on Device 63.

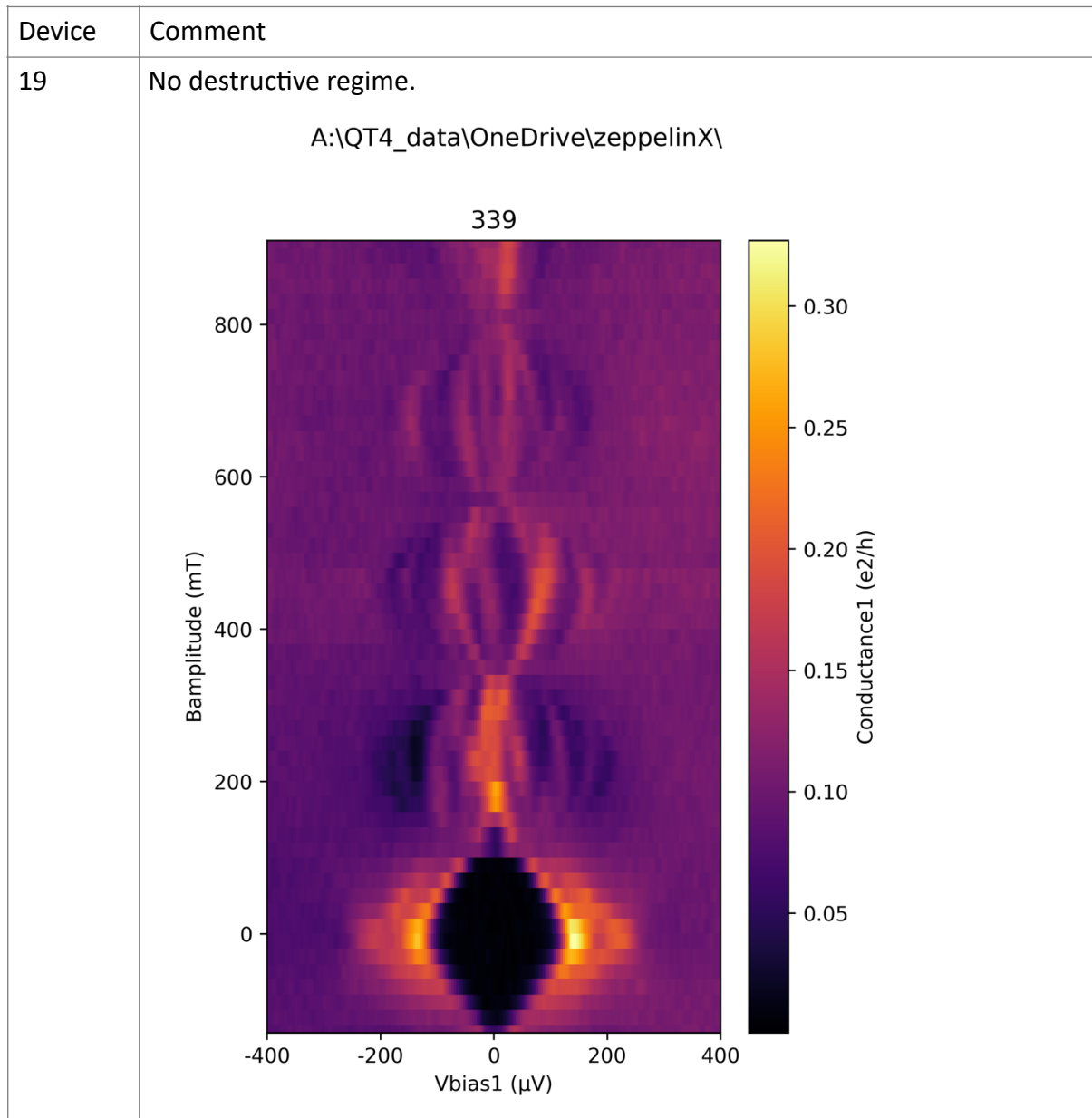
Devices 62, 67, and 69 are 4-probe devices.

General comment: A different wire batch (QDev829) than the main batch (QDev439) studied in the paper. The wide distribution of diameters in this batch resulted in the first lobe position ranging from ~200 to 600 mT for different devices. No systematic behavior was observed.

*See "Table PNS".

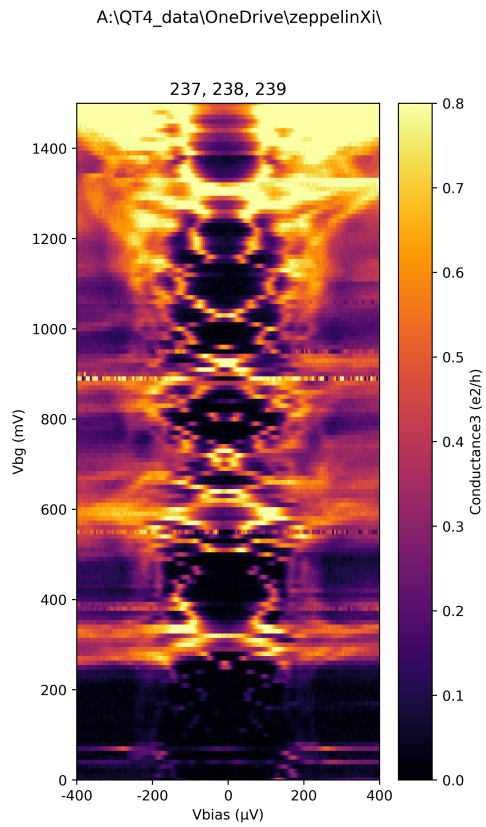
Table: Clear Spectroscopy, Procedure not satisfied (PNS), no ZBP.

QDev637



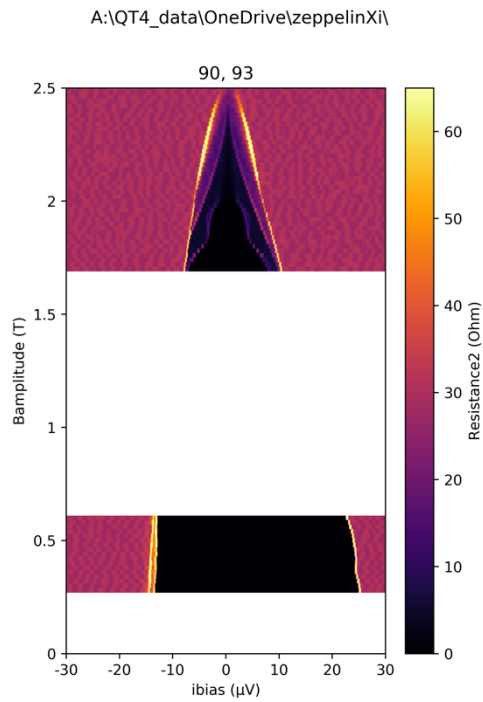
25

No tunneling regime.



26

4-probe data from this device did not show Little-parks lobe structure. The tunneling spectroscopy was not measured.

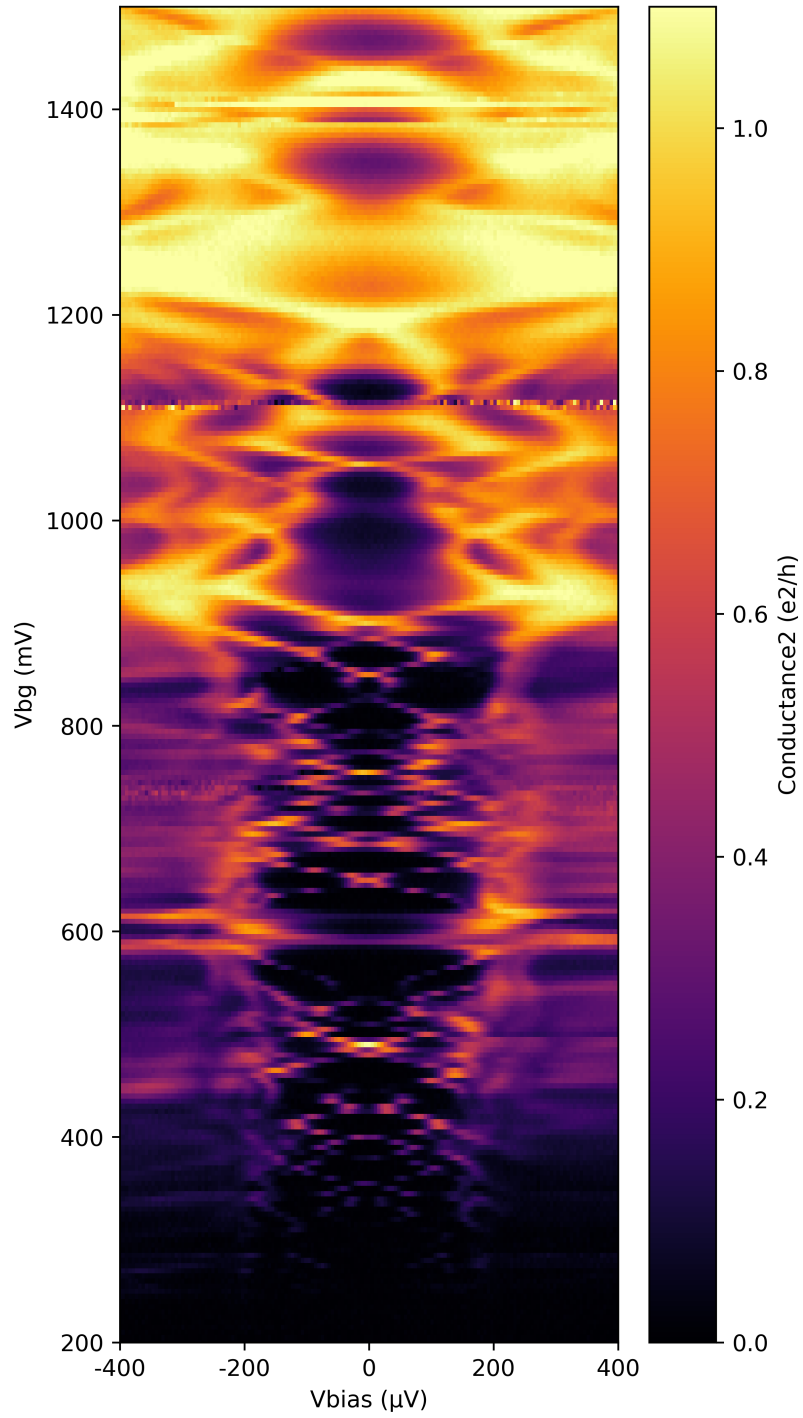


27

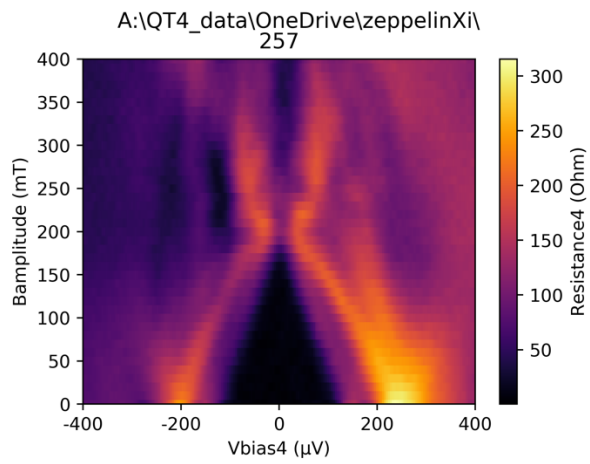
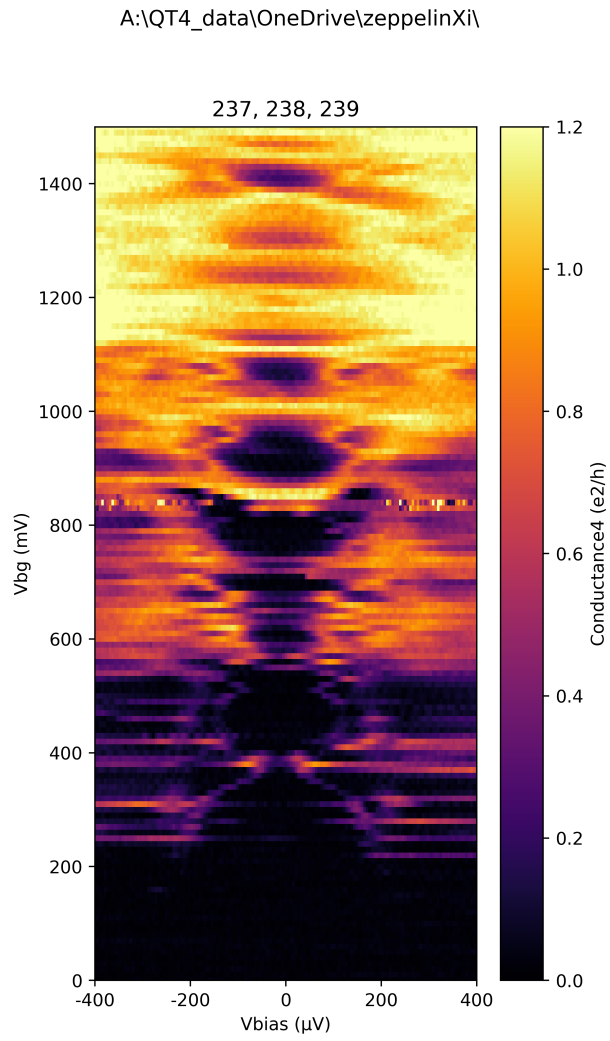
No tunneling regime.

A:\QT4_data\OneDrive\zeppelinXi\

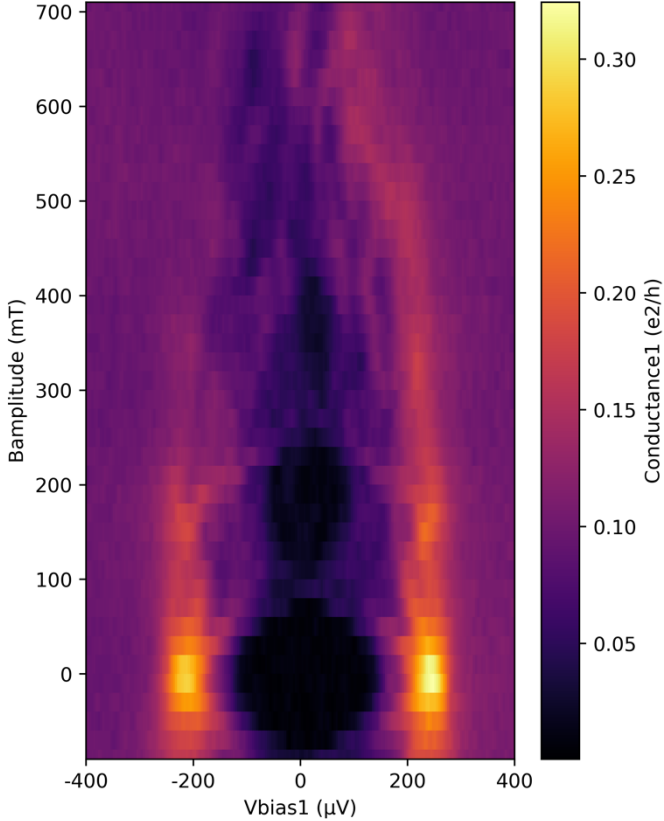
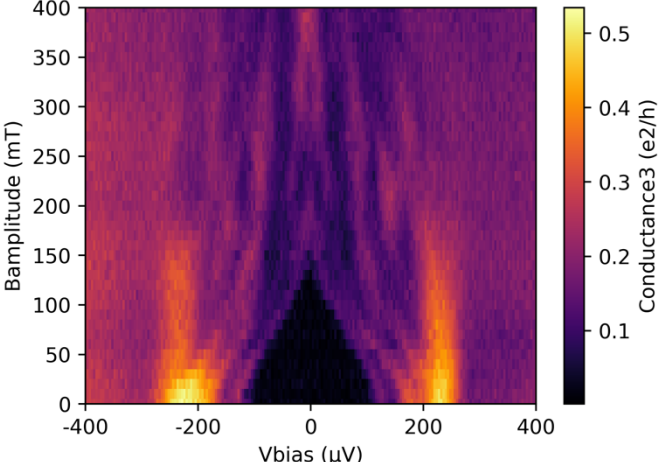
457, 459



No tunneling regime and washed out Little Parks lobe structure.

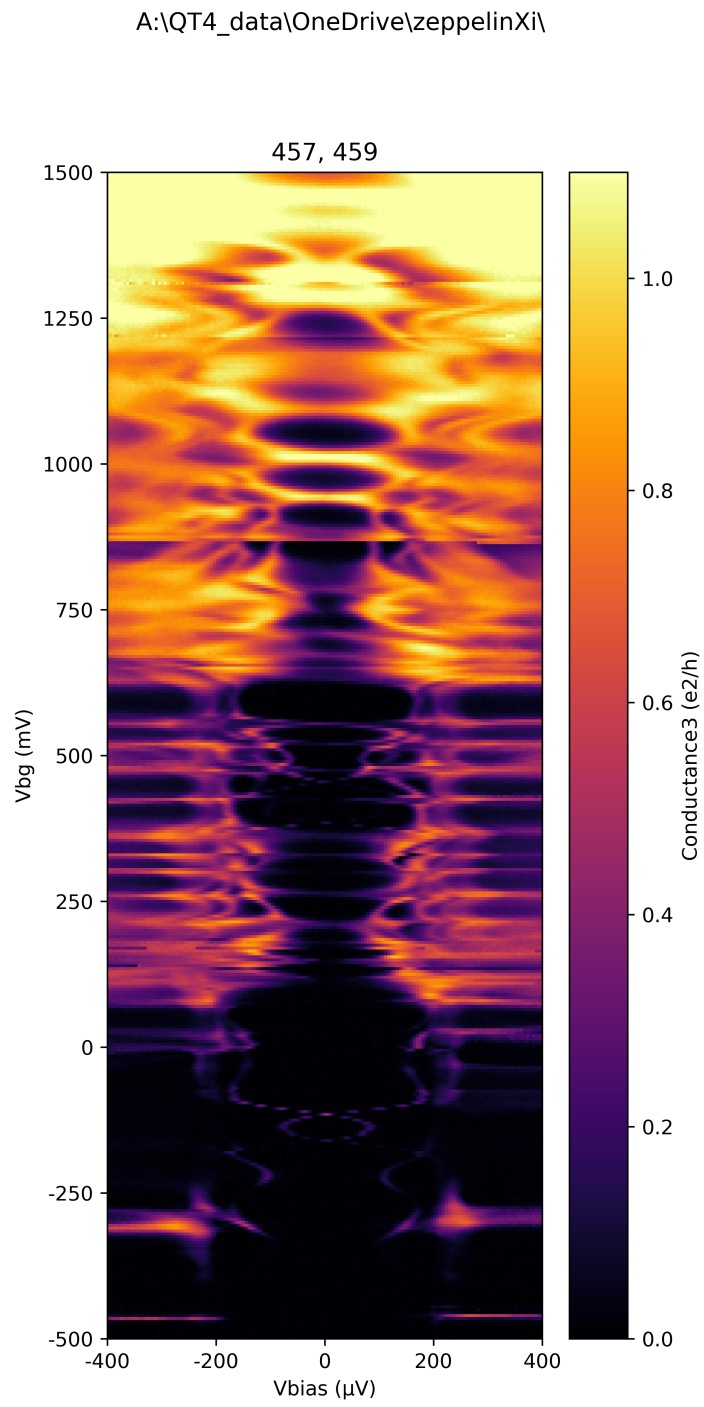


QDev638

Device	Comment
21	<p>Washed-out Little-Parks lobes. Clearly no destructive regime.</p> <p>A:\QT4_data\OneDrive\zeppelinX\ 374</p> 
31	<p>Washed out Little Parks lobe structure.</p> <p>A:\QT4_data\OneDrive\zeppelinXi\ 388</p> 

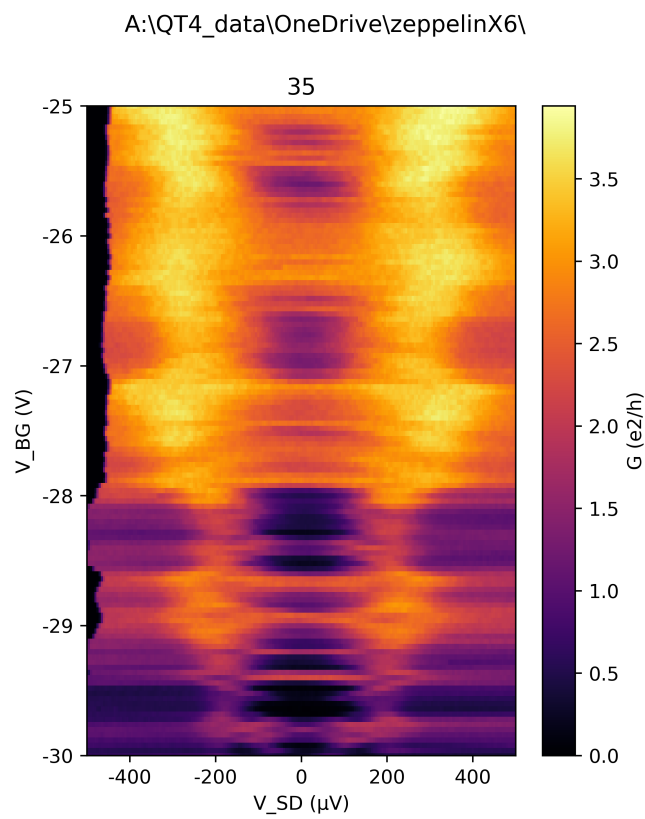
32

No tunneling regime.



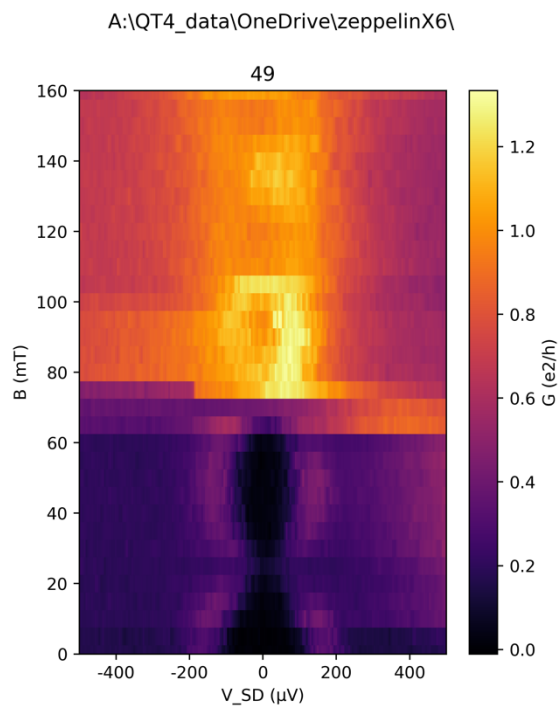
71

No tunneling regime.



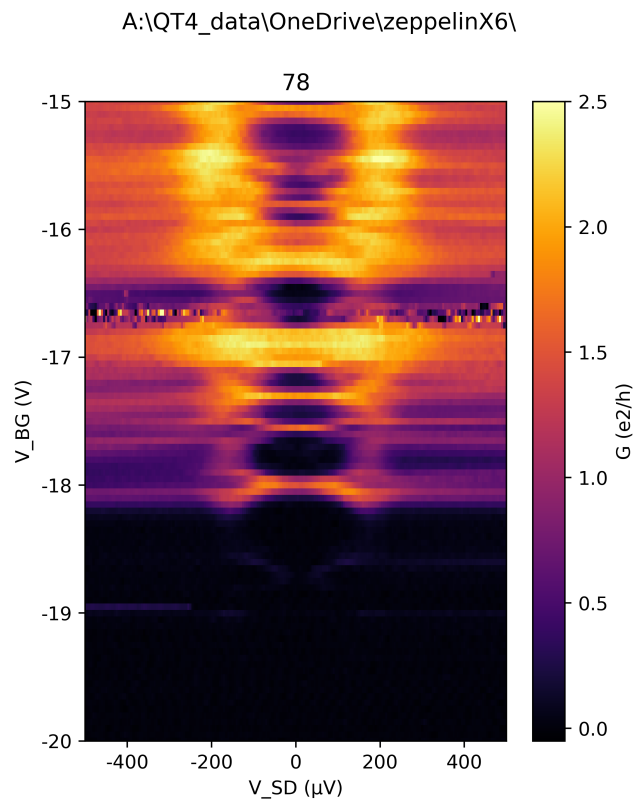
72

Washed out Little Parks lobe structure.



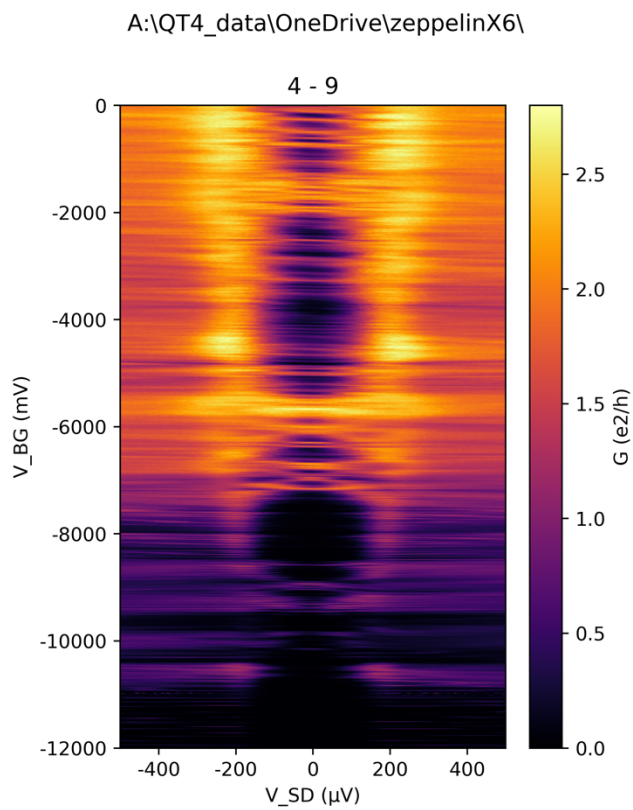
74

No tunneling spectroscopy.



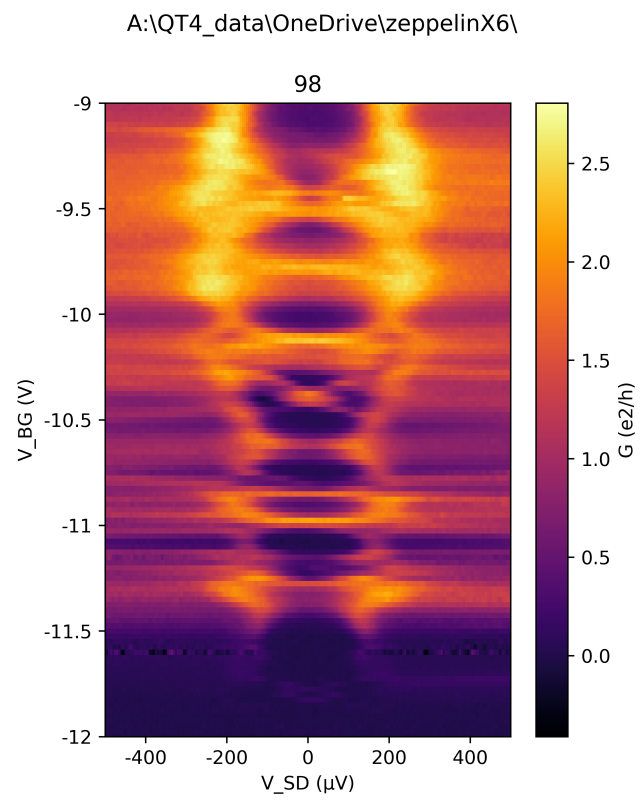
76

No tunneling regime.



77

No tunneling regime.



63

No tunneling regime.

A:\QT4_data\OneDrive\zeppelinX5\

